Mantle dynamics beneath the East Pacific Rise at 17°S: Insights from the Mantle Electromagnetic and Tomography (MELT) experiment

Kiyoshi Baba,[1,2] Alan D. Chave,[3] Rob L. Evans,[3] Greg Hirth,[3] and Randall L. Mackie[4]

Received 24 December 2004; revised 13 September 2005; accepted 4 November 2005; published 17 February 2006.

[1] The electromagnetic data from the Mantle Electromagnetic and Tomography (MELT) experiment are inverted for a two-dimensional transversely anisotropic conductivity structure that incorporates a correction for three-dimensional topographic effects on the magnetotelluric responses. The model space allows for different conductivity values in the along-strike, cross-strike, and vertical directions, along with imposed constraints of model smoothness and closeness among the three directions. Anisotropic models provide a slightly better fit to the data for a given level of model smoothness and are more consistent with other geophysical and laboratory data. The preferred anisotropic model displays a resistive uppermost 60-km-thick mantle independent of plate age, except in the vicinity of the ridge crest. In most inversions, a vertically aligned sheet-like conductor at the ridge crest is especially prominent in the vertical conductivity. Its presence suggests that the melt is more highly concentrated and connected in the vertical direction immediately beneath the rise axis. The melt zone is at least 100 km wide and is asymmetric, having a greater extent to the west. Off-axis, and to the east of the ridge, the mantle is more conductive in the direction of plate spreading at depths greater than 60 km. The flat resistive-conductive boundary at 60 km agrees well with the inferred depth of the dry solidus of peridotite, and the deeper conductive region is consistent with the preferred orientation of olivine inferred from seismic observations. This suggests that the uppermost 60 km represents the region of mantle that has undergone melting at the ridge and has been depleted of water (dissolved hydrogen). By contrast, the underlying mantle has retained a significant amount of water.

Citation: Baba, K., A. D. Chave, R. L. Evans, G. Hirth, and R. L. Mackie (2006), Mantle dynamics beneath the East Pacific Rise at 17°S: Insights from the Mantle Electromagnetic and Tomography (MELT) experiment, *J. Geophys. Res.*, *111*, B02101, doi:10.1029/2004JB003598.

1. Introduction

[2] The Mantle Electromagnetic and Tomography (MELT) experiment was undertaken to map the distribution of melt from its sources deep within the upper mantle to its eruption at a mid-ocean ridge [*MELT Seismic Team*, 1998; *Evans et al.*, 1999]. The experiment focused on the super fast spreading segment of the southern East Pacific Rise at 17°S using a combination of seafloor passive seismic and electromagnetic measurements over a period of about one year. One of the primary goals of the MELT experiment was distinguishing between competing classes of models for melt generation and mantle flow beneath mid-ocean ridges. Broadly speaking, these model classes can be separated into those which are controlled by a passive mantle response to plate spreading and those in which melt buoyancy and other dynamic forces contribute to the pattern of melt migration toward the ridge crest. In the passive flow models [e.g., *Spiegelman and McKenzie*, 1987; *Scott and Stevenson*, 1989], viscous drag from the separating plates induces a broad zone of upwelling and melt production that may be as wide as 100 km at a depth of 70 km beneath the seafloor. By contrast, the forces involved in dynamic flow models combine to focus upwelling and melting into a narrow zone a few kilometers to a few tens of kilometers across centered at the ridge crest [e.g., *Buck and Su*, 1989; *Braun et al.*, 2000].

[3] The conductivity of mantle materials depends strongly on temperature, on composition (including the degree of mantle hydration) and on the melt fraction, provided that the melt forms an interconnected network. The subsolidus conductivity of dry mantle rocks is a strong function of temperature, and has been accurately determined

[1]Institute for Research on Earth Evolution, Japan Agency for Marine-Earth Science and Technology, Yokosuka, Kanagawa, Japan.
[2]Now at Earthquake Research Institute, University of Tokyo, Tokyo, Japan.
[3]Woods Hole Oceanographic Institution, Woods Hole, Massachusetts, USA.
[4]GSY-USA, Inc., San Francisco, California, USA.

0148-0227/06/2004JB003598$09.00

in the laboratory [e.g., *Constable et al.*, 1992; *Xu et al.*, 2000]. The conductivity of old, cold, dry oceanic lithosphere is extremely low ($<10^{-5}$ S m^{-1}), but increases with depth in the mantle as temperature increases. The conductivity of olivine is thought to be enhanced by the presence of water in the form of dissolved hydrogen [*Karato*, 1990]. Although definitive laboratory measurements have yet to be made on olivine that quantify the impact of water on conductivity, enhanced values have been seen in wet samples of wadseleyite and ringwoodite [*Huang et al.*, 2005]. While dry olivine is only weakly electrically anisotropic, with the maximum conductivity oriented along the *c* axis, the diffusion of hydrogen in olivine is highly anisotropic suggesting that the conductivity should be similarly anisotropic with a maximum conductivity along the *a* axis [*Kohlstedt and Mackwell*, 1998]. The intrinsic conductivity of basaltic melt is many orders of magnitude higher than that of host mantle rock [*Roberts and Tyburczy*, 1999], but the manner in which partial melting impacts bulk conductivity depends on the geometry and connectedness of melt pockets. Partially molten mantle can also be electrically anisotropic, depending on the preferred orientation of the melt fabric.

[4] Analysis of the MELT seismic and electromagnetic data has been ongoing since completion of the experiment in 1996 (seismic component) and 1997 (electromagnetic (EM) component), and published results reveal a striking asymmetry between the mantles beneath the Pacific and Nazca plates [e.g., *MELT Seismic Team*, 1998; *Evans et al.*, 1999] which is also manifest in surface morphology [*Scheirer et al.*, 1998] and plate motion [*Small and Danyushevsky*, 2003]. The pattern of *P* and *S* wave delays shows a clear cross-ridge difference in which the average *S* wave gradient is about twice as large on the east as on the west side [*Toomey et al.*, 1998]. Both body wave and Rayleigh wave patterns display minimum velocities offset to the west of the southern East Pacific Rise [*Toomey et al.*, 1998; *Forsyth et al.*, 1998]. Recent work has extended the analysis of short-period Love waves [*Dunn and Forsyth*, 2003], teleseismic *P* and *S* arrivals [*Hammond and Toomey*, 2003], and Rayleigh waves to further constrain the mantle structure. *Dunn and Forsyth* [2003] obtained models that extend from the base of the crust downward, and show that, although less pronounced, the mantle structure is asymmetric even at these shallow depths.

[5] Inversion of the magnetotelluric response functions for an isotropic electrical structure also show an asymmetric mantle, with a broad region of enhanced conductivity in the uppermost 100 km to the west of the ridge that is not observed to the east [*Evans et al.*, 1999]. The conductivity in the upper 60 km east of the ridge is consistent with a dry olivine mineralogy, indicating a mantle depleted of melt and water. However, other features in the isotropic model of the MELT data, as well as issues raised through analysis of the two data polarizations suggest the presence of significant electrical anisotropy [*Chave et al.*, 2001].

[6] In this paper, the results from further modeling of the MELT EM data using two new procedures and incorporating additional measurements are described. The first of these is detailed correction of the data for the effects of seafloor topography [*Baba and Chave*, 2005]. The other advance is two-dimensional (2-D) inversion for transversely anisotropic conductivity structure where previous work imposed electrical isotropy.

[7] The remainder of this paper is divided into six sections. Section 2 describes the data and their processing, while section 3 gives an overview of the topographic stripping algorithm which is fully described by *Baba and Chave* [2005]. Section 4 presents the anisotropic inversion algorithm along with a representative suite of isotropic and anisotropic results from the MELT data. Section 5 describes tests for significance applied to major features observed in these models. The major features of the models are interpreted in section 6.

2. Data and Data Processing

[8] Measurements of the electric and magnetic field time variations were acquired along two transects extending several hundred kilometers to either side of the southern East Pacific Rise and oriented perpendicular to regional strike. These data were processed into the frequency- and site-dependent tensors relating the horizontal electric and magnetic field variations using a remote reference, bounded influence algorithm described by *Chave and Thomson* [2003, 2004]. The jackknife method [*Thomson and Chave*, 1991] was used to derive accurate uncertainty estimates on the tensor elements.

[9] Figure 1 shows the regional bathymetry along with the EM measurement sites. This study focuses on the main southern line, which crosses the southern East Pacific Rise at 17°S, where the wide axial morphology is suggestive of an abundant magma supply. The line consists of 19 sites collected by investigators from four countries and extending 200 km on either side of the ridge crest. Owing to instrument failures and losses, full magnetotelluric (MT) response functions were recovered at only 13 sites. Most of these losses occurred at the western end of the profile, limiting ability to constrain structure beneath the off-axis Pacific plate. In some cases, loss of an electric field sensor meant that the MT tensor transfer function was calculated using electric field data from an adjacent site. In general, this is not a significant problem as the seafloor magnetic field varies with position more rapidly than the electric field does, and hence contains more information about the underlying structure. This is opposite to the sense for MT data on land, for which the magnetic field is usually more slowly varying with location. In any case, the actual location of the electric and magnetic field measurements was accounted for during modeling and inversion. Table 1 lists site information, including the combination of electric and magnetic field data used for estimation of the MT response. In addition to the measurements included by *Evans et al.* [1999], three additional MT responses at sites F, H, and R were employed as data problems were overcome.

[10] Over a 2-D resistivity structure, the MT response may be described by two independent modes. These correspond to electric currents that flow either parallel to the regional strike (transverse electric or TE mode) or in vertical loops whose plane is oriented perpendicular to strike (transverse magnetic or TM mode). When the horizontal coordinate system is rotated so that the *x* axis is parallel to the strike direction, the diagonal elements of the MT tensor

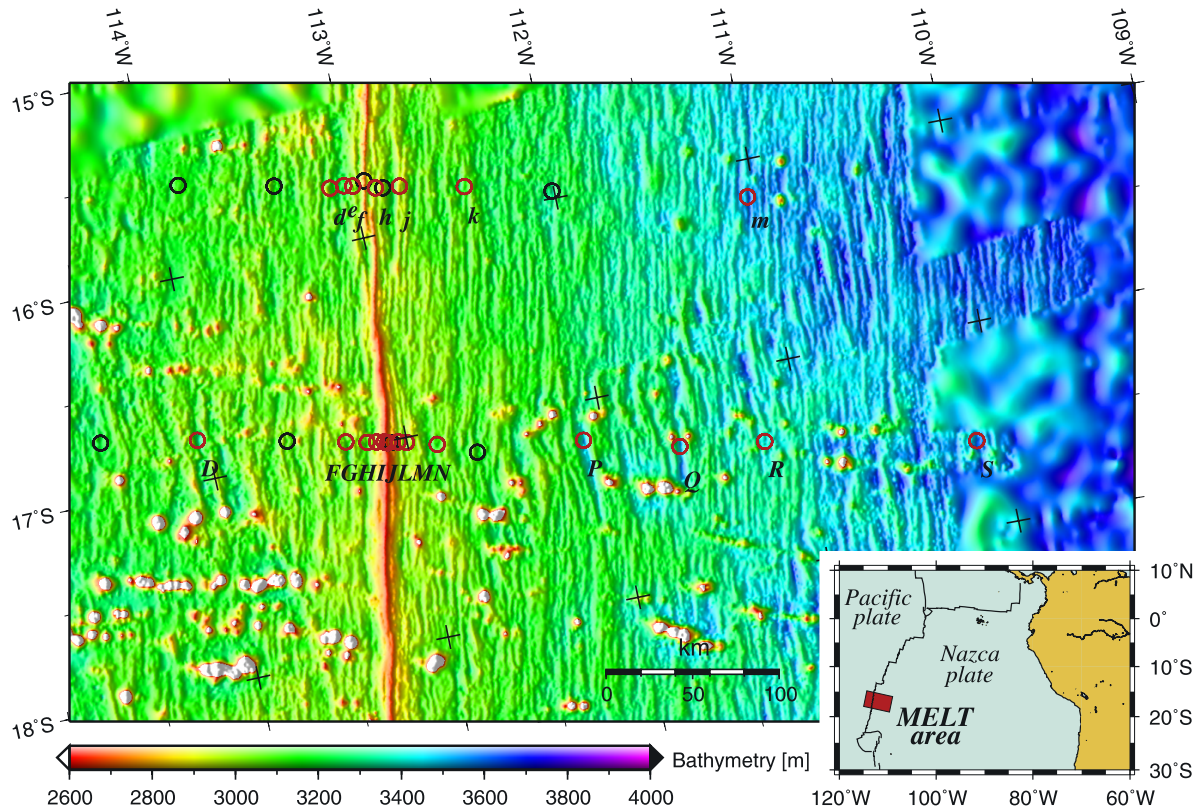

Figure 1. Location of the MELT EM sites superimposed on a bathymetric map (circles). The bathymetry data were obtained by combining multibeam data on a 1 km mesh [*Scheirer et al.*, 1998] with coarser predicted bathymetry (2′ mesh) from *Smith and Sandwell* [1994]. Red circles with labels are the sites where MT responses were used in this paper.

Z vanish and the off-diagonal elements Z_{xy} and Z_{yx} correspond to the TE and TM modes, respectively. In general, the TE mode is especially sensitive to continuous conductive features oriented in the strike direction, while the TM mode is sensitive to the background layered conductivity structure and also to resistivity boundaries which alter cross-ridge electric current flow [e.g., *Wannamaker et al.*, 1989; *Evans and Everett*, 1992]. The two modes also respond differently to transverse anisotropy. Thus each mode contains complementary information about mantle structure which can be elucidated by inverting the two modes separately and together.

[11] The measured MT tensors display most of the characteristics of a 2-D medium, including weak diagonal elements relative to the off-diagonal ones. Although the possibility of 3-D effects cannot be ruled out, for 2-D analyses the strike direction can be regarded as that of the southern East Pacific Rise, so that to lowest order the structure is unchanged along strike.

3. Topographic Stripping

[12] The seafloor electromagnetic fields measured in the MELT experiment are strongly distorted by the rugged mid-ocean ridge bathymetry, and especially by local features such as fault-controlled valleys and seamounts which occur throughout the region. Bathymetric distortion is usually dominantly galvanic (i.e., due to the frequency-independent, quasi-static effect of electric charge) rather than inductive (i.e., due to the frequency-dependent effect of induced electric currents). In either case, topography presents significant modeling difficulty, as it is numerically difficult to simultaneously resolve the small-scale (relative to the induction scale) bathymetry that produces distortion and yet include the much larger-scale heterogeneous structure of the underlying mantle. The now standard approach to this problem in MT is the application of a tensor decomposition model [e.g., *Groom and Bailey*, 1989; *Chave and Smith*, 1994] to the observed responses to remove galvanic and

Table 1. Available Data From the Southern Line

Site	Distance From the Ridge Axis, km	Depth, m	Available Field Components	Combination (*E* Site/*M* Site)
D	−102.8	3346	*E*, *M*	D/D
F	−21.9	3084	*M*	I/F
G	−10.4	3167	*M*	I/G
H	−5.2	2817	*M*	I/H
I	−1.0	2636	*E*, *M*	I/I
J	1.0	2738	*M*	I/J
L	6.6	3022	*E*, *M*	L/L
M	11.2	3020	*E*, *M*	M/M
N	27.9	3126	*M*	L/N
P	107.7	3588	*E*, *M*	P/P
Q	160.3	3538	*M*	S/Q
R	206.8	3472	*M*	S/R
S	322.3	3610	*E*, *M*	S/S

inductive distortion due to small-scale features and recover the regional response which reflects mantle structure. However, these methods frequently fail to yield a statistically acceptable fit to seafloor data at all periods, suggesting a breakdown of the tensor decomposition model assumptions. This type of decomposition method was applied to the MELT data by *Evans et al.* [1999], but it failed for many sites and was not further considered.

[13] *Evans et al.* [1999] adopted two complementary approaches to deal with electromagnetic distortion. In the first, the observed MT responses were directly inverted to yield a model which includes simplified 2-D topography incorporating only the axial high and thermal subsidence with crustal age. In the other approach, 3-D topographic effects were first stripped from the observed MT responses by calculating the effect of topography using a variable conductance thin sheet to simulate areas of laterally varying resistive seafloor and conductive seawater, as originally described by *Nolasco et al.* [1998]. Subsequently, the corrected responses were inverted. However, the thin sheet approximation is increasingly inaccurate at periods under 1000 s, so that short-period correction becomes problematic. At the time, these two approaches were state of the art and also yielded similar inversion models, suggesting that the results were not seriously biased by the underlying assumptions. However, a new and more complete approach to stripping topography has recently been developed [*Baba and Seama*, 2002; *Baba and Chave*, 2005], and this has been applied to the MELT data prior to inversion. This new algorithm allows more precise stripping of topographic effects from the MELT data at all recorded periods, especially those under 1000 s where the effect is especially significant.

[14] The new approach to correction for topography is only summarized here; the reader is referred to *Baba and Chave* [2005] for a complete description, including details of the grids used to correct the MELT data. It is assumed that the effect of topography can be expressed as a complex distortion tensor multiplying the undistorted MT response, so that

$$\mathbf{Z} = \mathbf{Z}_t \mathbf{Z}_m, \tag{1}$$

where $\mathbf{Z}$ is the full (distorted) MT tensor, $\mathbf{Z}_t$ quantifies the topographic distortion, and $\mathbf{Z}_m$ is the response due solely to the underlying regional structure. In a numerical context, $\mathbf{Z}$ and $\mathbf{Z}_m$ can be calculated from an assumed mantle structure, allowing $\mathbf{Z}_t$ to be estimated. Defining the observed response $\mathbf{Z}_o$ and the topographically corrected response $\mathbf{Z}_c$ analogously to $\mathbf{Z}$ and $\mathbf{Z}_m$, respectively, the observed response may be corrected as follows:

$$\mathbf{Z}_c = \mathbf{Z}_t^{-1}\mathbf{Z}_o = \left(\mathbf{Z}\mathbf{Z}_m^{-1}\right)^{-1}\mathbf{Z}_o = \mathbf{Z}_m\mathbf{Z}^{-1}\mathbf{Z}_o. \tag{2}$$

For the forward calculation, the numerical modeling method of *Baba and Seama* [2002], which includes 3-D topography over an arbitrary underlying mantle structure, was utilized. The method overcomes the difficulty of direct modeling of topography by its transformation into lateral anisotropic conductivity and magnetic permeability changes within the elements in two layers bounding a flattened seafloor. This approach results in a considerable saving in the required number of vertical grid cells. The coupling of deep structure to surface topography may be checked by iteratively updating the mantle structure at each step.

Table 2. Initial 1-D Resistivity Model for the Topographic Effect Correction

Depth, km	Resistivity, Ω m
0.00–3.20	0.3125
3.20–9.39	1000.0
9.39–51.49	5000.0
51.49–393.29	50.0
>393.29	1.0

[15] For application to the MELT data, an area of 4032 × 4320 km centered on the survey line was discretized and modeled at once for all of the sites. The grid mesh used to correct the data is finer (1–2 km grid spacing) around each observation site, and becomes coarser further away to save computer memory. Therefore both the small-scale local topography and large-scale regional effects like thermal subsidence may be taken into account.

[16] The corrected responses of the Z_{xy} and Z_{yx} elements change smoothly with period except for one or two data points at most of the sites. These few outliers were cleaned using the ρ^+ algorithm of *Parker and Booker* [1996], which places lower and upper bounds on the apparent resistivity and phase consistent with the governing physical dispersion relation. For sites F and R, which were not included in the previous study of *Evans et al.* [1999], the apparent resistivities display a few unusual features compared with those at other sites, possibly because of instrumental problems. At these sites, the apparent resistivities at the shorter periods were shifted to achieve consistency with the phases, making their errors larger.

[17] At this point, the data are considered ready for inversion. However, the full topographic effect is dependent on the underlying mantle structure, and hence at each step in the inversion algorithm, the responses must be recorrected. The correction algorithm is initialized with the 1-D layered structure given in Table 2. This model was obtained by approximating the 2-D resistivity model of *Evans et al.* [1999] using four layers and is compatible with estimates of the resistivity of the oceanic lithosphere and asthenosphere from other studies [e.g., *Heinson and Lilley*, 1993; *Lizarralde et al.*, 1995; *Nolasco et al.*, 1998]. The impact of coupling between the underlying mantle and the topography was tested by running two iterations of the topographic stripping and the 2-D inversion. The RMS misfit between the observed responses and those calculated from the forward model (mantle + topography) varied with iteration number as shown in Table 3. As discussed by *Baba and Chave* [2005], the RMS misfit was reduced significantly at the end of the first iteration, but did not decrease significantly as a result of the second. This means that the electromagnetic coupling between topography and the mantle is not strong in the MELT area. Therefore, in the inversion results described in the next sections, only one stripping and inversion step was utilized.

[18] The effects of the topographic correction on the data are shown in Figure 2 which shows the response tensor for

Table 3. RMS Misfit Between Observed and Calculated MT Responses

	RMS Misfit	
Iteration	*xy*	*yx*
0	6.960	9.074
1	3.949	5.244
2	3.985	11.137

sites I and Q. Site I is located on the axial high, and significant topographic effects are seen in both the apparent resistivity and phase of the TE mode response at short periods and in the TM mode apparent resistivity, which is shifted independently of period. The responses for the Z_{xy} and Z_{yx} elements are close to each other at long (>10,000 s) periods, but the responses are split at shorter ones. This behavior is also seen at site J, which was located on the axial high, but becomes weaker with increasing distance away from the ridge axis. The shift of the TM mode apparent resistivity at site I is due to galvanic effects, probably from the strong axial high. Site Q is in a ridge-parallel valley 160 km to the east of the ridge axis and close to two seamounts. The apparent resistivity of both the TE and TM modes splits in the midperiod (2000–20,000 s) range, and is little changed after application of the topographic correction, while the phases, which increase to over 90 degrees at the shortest periods measured, are changed substantially by the correction.

4. Inversion for Anisotropic Structure

4.1. Motivation for the Introduction of Anisotropy

[19] There are suggestions from isotropic inversion that anisotropic resistivity structure is present beneath the southern East Pacific Rise. There are persistent problems with the application of an isotropic MT inversion to anisotropic responses that can lead to physically implausible structures, as demonstrated by *Chave et al.* [2001]. Key among these is a narrow, highly conductive feature at the ridge crest that is apparent in an isotropic joint inversion, but which does not appear in separate isotropic inversions for the TE and TM modes. *Evans et al.* [1999] also describe a region 300 to 400 km to the east of the East Pacific Rise where the conductivity is higher than that in the model of *Lizarralde et al.* [1995], which represents an average structure for the Pacific plate. *Evans et al.* [1999] speculated that this enhanced conductivity is the result of strain-induced anisot-

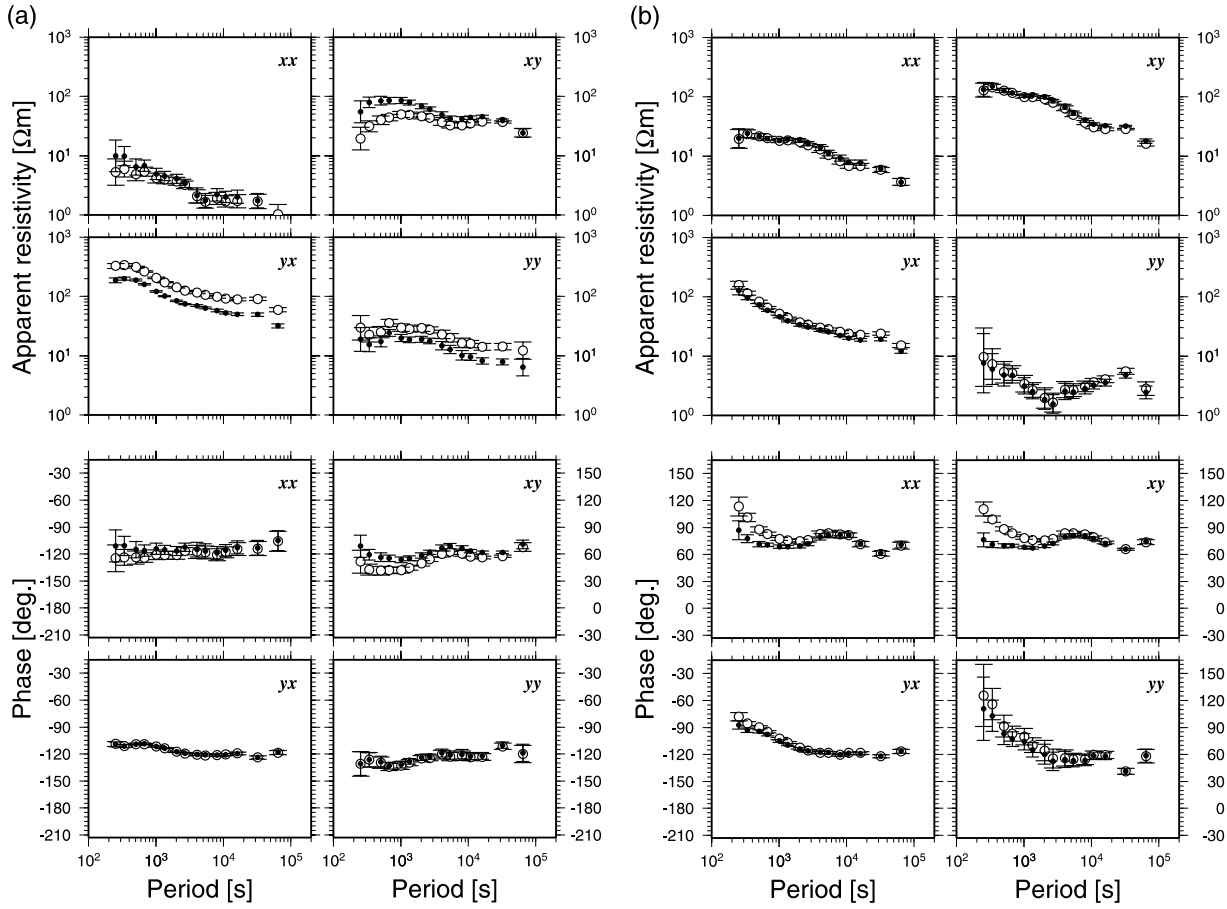

Figure 2. Apparent resistivity and phase tensors at (a) site I and (b) site Q. The *x* and *y* axes are oriented along and across the East Pacific Rise, respectively. White circles are the observed responses and black circles are the responses after topographic correction. Error bars indicate double-sided 95% confidence levels.

ropy in olivine that contains water in the form of dissolved hydrogen.

[20] In addition, there are features beneath the ridge crest that might be expected to show anisotropy. A major example occurs near the rise axis, where melt is likely to be preferentially oriented along vertical pathways. The possibility of imaging such a feature (which would have a significant impact on the vertical flow of electric current) partially motivates the analysis presented in this paper.

4.2. Anisotropic Inversion Algorithm

[21] In the presence of anisotropy, the standard TE and TM mode descriptions for a 2-D structure must be modified. If the anisotropy is oriented with the regional strike, so that the conductivity tensor can be represented only by its three diagonal elements, then the equations for the TE mode will remain the same as for a 2-D medium, with the electromagnetic field dependent on the along-strike conductivity, but the TM mode will involve both the σ_{yy} and σ_{zz} components, and as a consequence will be different from the isotropic expression in the event that σ_{yy} differs from σ_{zz} (equations (3)–(4)). In addition, the TE and TM modes are sensitive to different horizontal conductivities, which in most but not all cases are expected to dominate over the vertical component.

[22] The 2-D MT inversion algorithm based on the nonlinear conjugate gradient method of *Rodi and Mackie* [2001] was modified to incorporate anisotropic conductivity structure where the conductivity is expressed as a diagonal second rank tensor. This approximation is supported by evidence from seismic SKS splitting data [*Wolfe and Solomon*, 1998], which display alignment of mantle fabric perpendicular to the spreading axis. In this instance, the TE and TM modes are governed by

$$\frac{\partial^2 E_x}{\partial y^2}+\frac{\partial^2 E_x}{\partial z^2}+i\omega\mu\sigma_{xx}E_x=0 \tag{3}$$

$$\frac{\partial}{\partial y}\left(\rho_{zz}\frac{\partial H_x}{\partial y}\right)+\frac{\partial}{\partial z}\left(\rho_{yy}\frac{\partial H_x}{\partial z}\right)+i\omega\mu H_x=0, \tag{4}$$

respectively, where x, y, z are the along-strike, cross-strike, and vertical (positive downward) directions, E_x (H_x) are the x components of the electric (magnetic) field, ω is angular frequency, μ is the magnetic permeability of free space, and σ is the electrical conductivity (ρ is the resistivity which is the inverse of conductivity) which has three direction-dependent elements.

[23] The inverse problem is solved by regularization through minimizing an objective function, Φ, defined by

$$\begin{aligned}\Phi(m) = {} & (\mathbf{d}-F(\mathbf{m}))^t\mathbf{V}^{-1}(\mathbf{d}-F(\mathbf{m}))\\ & +\tau_s(\mathbf{m}-\mathbf{m}_0)^t\mathbf{L}_s^t\mathbf{L}_s(\mathbf{m}-\mathbf{m}_0)\\ & +\tau_c\mathbf{m}^t\mathbf{L}_c^t\mathbf{L}_c\mathbf{m},\end{aligned} \tag{5}$$

where $\mathbf{d}$ is the observed data vector, F is the forward modeling operator, $\mathbf{m}$ is the unknown model vector, $\mathbf{m}_0$ is the a priori model vector, $\mathbf{V}$ is the error covariance matrix, $\mathbf{L}_s$ and $\mathbf{L}_c$ are linear operators expressing imposed constraints, and τ_s and τ_c are regularization parameters for the smoothness (subscript s) and degree of anisotropy (subscript c). The model vector is the log of the anisotropic resistivity as a function of position:

$$\mathbf{m}(y,z)=\ln\begin{bmatrix}\rho_{xx}(y,z)\\ \rho_{yy}(y,z)\\ \rho_{zz}(y,z)\end{bmatrix}. \tag{6}$$

[24] Two types of regularization have been imposed, as given by the second and third terms in the objective function. The second term controls model smoothness. The regularization operator $\mathbf{L}_s$ is chosen to be a second-derivative difference type which approximates the Laplacian of $\ln(\rho_{ii})$, where ii is xx, yy, or zz. The Laplacian derivative is weighted by the vertical grid size, which implicitly increases the penalty on the vertical roughness since the block thickness increases with depth, and also increases the penalty on the horizontal roughness with depth in a way that is consistent with the implicit increase in vertical roughness. This weighting is used to eliminate vertical stretching or unnecessary roughness that might otherwise ensue in the inversion model. As the smoothness parameter τ_s grows, the inversion forces the model to be less spatially rough. The third objective function term controls the closeness of the ρ_{xx}, ρ_{yy}, and ρ_{zz} models. As the anisotropy parameter τ_c increases, the inversion forces the model to be increasingly isotropic. If $\tau_c = 0$, the closeness is not constrained at all, and the three models become completely independent.

[25] As a test of compatibility with previous work, the TE and TM mode data were first jointly inverted for an isotropic structure by setting τ_c to a large value. These results (Figure 3a) and those of *Evans et al.* [1999] (Figure 3c) are broadly similar, and the small discrepancies between them are likely due to algorithmic differences, an improved ability to fit data that have been cleaned of topographic influence, and the introduction of three additional stations as previously described.

4.3. Anisotropic Inversion Results

[26] The inversion algorithm has been used to generate a suite of models that vary in smoothness parameter, τ_s, and in the degree of anisotropy parameter, τ_c. In addition, for each combination of regularization parameters, the inversion was carried out with four different starting models to verify proper convergence. All of the starting models are isotropic half-spaces, but their resistivities are 100, 50, 30, and 20 Ωm, respectively. Noise floors of 10% on the apparent resistivity and 3% ($\sim$0.87 degrees) on the phase were applied to all of the data for all inversion. As expected, more anisotropic and/or rougher models have a larger number of degrees of freedom and therefore provide a better fit to the data. The minimum RMS misfit is achieved for $\tau_s = 1$, $\tau_c = 0$ (this means that no constraint for closeness is applied, and hence the model is freely anisotropic), and a starting half-space resistivity of 20 Ωm. The best fitting model may not be the optimal choice, as such solutions generally overfit the data and include spurious structure. For example, in the rougher and more anisotropic parts of parameter space, the algorithm tends to introduce conductive bodies in the zones between sites where data sensitivity is low.

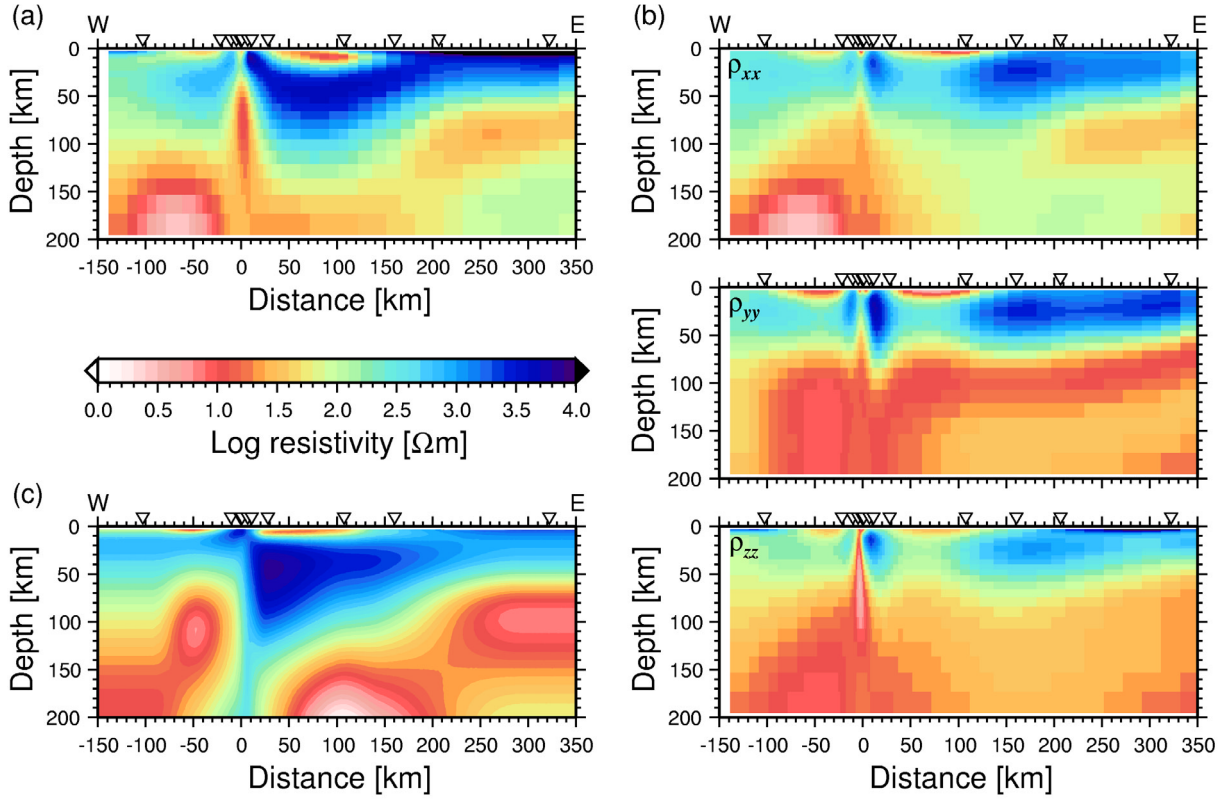

Figure 3. Two-dimensional resistivity (a) isotropic and (b) anisotropic models obtained using the anisotropic inversion in this study and (c) model presented by *Evans et al.* [1999]. Figure 3b (top) shows resistivity in the along-strike direction, and the middle and bottom panels show resistivities in the spreading direction and the vertical direction, respectively. The rise axis is located at 0 km on the horizontal axis, and triangles indicate the locations of the MT measurements.

[27] Figure 4 is a map of the RMS misfit as a function of τ_s and τ_c for the final suite of inversion models. The preferred models are chosen from the region of the misfit map in which the misfit is acceptable but is away from the steepest gradients in misfit with respect to τ_s and τ_c. For example, at $\tau_s = 0.3$ and $\tau_c = 0.01$, the misfit is about 2.3. Moving to the right along a line of constant closeness, the misfit slowly increases until it starts to change rapidly around $\tau_s = 1.0$. The fit for larger smoothness parameters is deemed unacceptable. In general, solutions with smoothness values around $\tau_s = 3$ are preferred, and the best model has $\tau_s = 3$ and a closeness parameter $\tau_c = 0.1$.

[28] The anisotropic model in (Figure 3b) for $\tau_s = 3$ and $\tau_c = 0.1$ has many features in common with the isotropic model obtained by *Evans et al.* [1999] (Figure 3c): principally, a structure that is asymmetric across the ridge axis, with higher conductivity to the west, especially in the upper 60 km. In addition, it has several key features that were either not seen in earlier isotropic solutions, or which could not be clearly identified owing to the assumption of isotropy. In particular, the model contains (1) a highly conductive region in the across-ridge (y) direction below ~60 km to the east of the rise; (2) a resistive-conductive boundary that is flat lying and independent of distance from the ridge axis, and (3) a narrow, vertically and along-strike-aligned conductive sheet in the vertical conductivity located beneath the rise axis which is also apparent in the across-ridge conductivity.

[29] The first and second features are consistent with other geological and geophysical observations, and are more readily interpretable than the corresponding features in the isotropic models. The third feature, a sheet-like conductor beneath the rise axis in ρ_{zz}, is probably the result of the high sensitivity of MT data to even weak vertical electrical connection between the highly conductive ocean and deep mantle. A vertical conductor would cause electric currents to turn from the base of the crust deeper into the mantle (or vice versa), and hence can strongly influence the TM mode data. Indeed, if there is electrical connection between the top of the sheet and the ocean, the effect will be profound, as demonstrated in modeling studies which preceded the MELT experiment [*Chave et al.*, 1992].

[30] The RMS misfit for the preferred anisotropic model is 2.44 compared to a value of 2.55 for the isotropic solution. Choosing the summary test statistic $V_i/V_a = 2.550^2/2.443^2 = 1.09$, where both numerator and denominator have 731 degrees of freedom, a two-sided F test for the null hypothesis that the variances of the isotropic and anisotropic models V_i and V_a are identical may be tested against the alternate hypothesis that they are not. Since the test statistic lies between the quantiles of the F distribution at the (0.025,0.975), (0.05,0.95), and (barely) at the

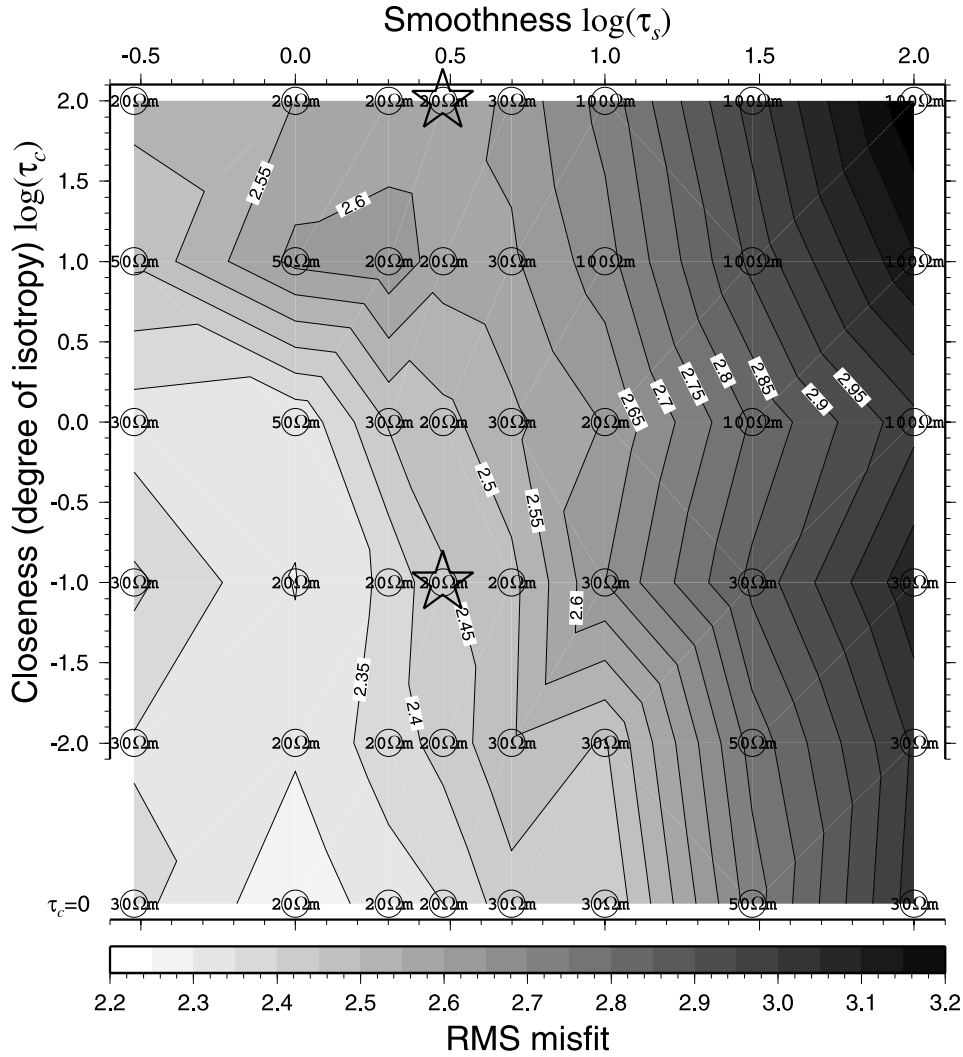

Figure 4. RMS misfit surface for various smoothness (horizontal axis) and closeness (vertical axis) parameters and for the preferred starting model. Note the use of a log scale for the horizontal and vertical axes. A larger value for the closeness parameter results in a more isotropic model, while a larger value for the smoothness parameter results in a smoother model. Circles are the points where a model was derived. The superimposed values are the resistivities of the starting half-space model for which the best fit was obtained. The two stars are the points for the preferred isotropic and anisotropic models shown in Figure 3.

(0.1,0.9) levels, the null hypothesis may be accepted at no more than a significance level of 0.8. The difference in RMS misfit alone is too small to allow selection of the anisotropic model over the isotropic solutions at standard significance levels. Pseudosections of the responses calculated from the isotropic and anisotropic models visually demonstrate the similarity in fit (Figure 5).

5. Test for the Significance of Major Features

[31] A series of tests were carried out to identify features that are required by the data. These tests were initiated through a formal sensitivity analysis which identifies those aspects of the anisotropic model to which the data are most sensitive. A contour map of sensitivity (defined by the diagonal elements of the sensitivity matrix $\mathbf{A}^t\mathbf{V}^{-1}\mathbf{A}$, where $\mathbf{A}$ is the Jacobian matrix and $\mathbf{V}$ is the error covariance matrix) is shown in Figure 6. The sensitivity is a measure of the extent by which a change in a model parameter results in a change in the MT response at the seafloor. A large excursion in the model response due to a change in a model parameter indicates high sensitivity to that feature, although the test is a local perturbation around the model value and does not account for global nonuniqueness. In Figure 6, log sensitivity values greater than -1, corresponding to MT response changes over 10%, will be considered significant. This choice is conservative, and in reality changes that are 1/2 to 1/3 of this value can be detected. The data are most sensitive to the conductive region east of the ridge and below 60 km which has a higher value in the direction of plate spreading (ρ_{yy}). The data are also sensitive (albeit less so) to the along-strike conductivity (ρ_{xx}) in the same region, suggesting that the data are sensitive to electrical anisotropy in this portion of the mantle.

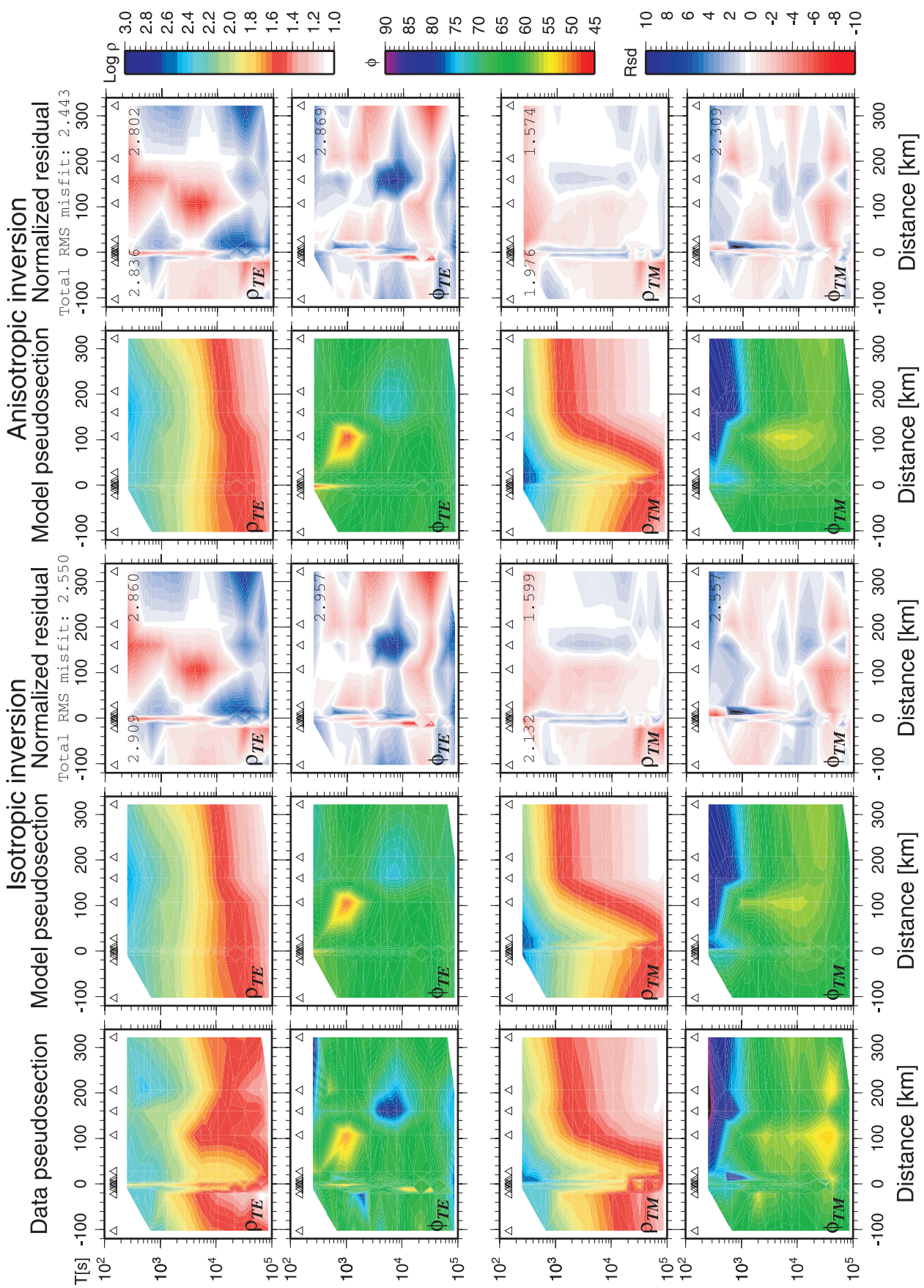
Isotropic inversion
Anisotropic inversion
Data pseudosection
Model pseudosection
Normalized residual
Model pseudosection
Normalized residual
Total RMS misfit: 2.550
Total RMS misfit: 2.443
T[s]
Distance [km]
Log ρ
ϕ
Rsd
2.909
2.860
2.957
2.836
2.802
2.869
2.132
1.599
2.557
1.976
1.574
2.309

Figure 5

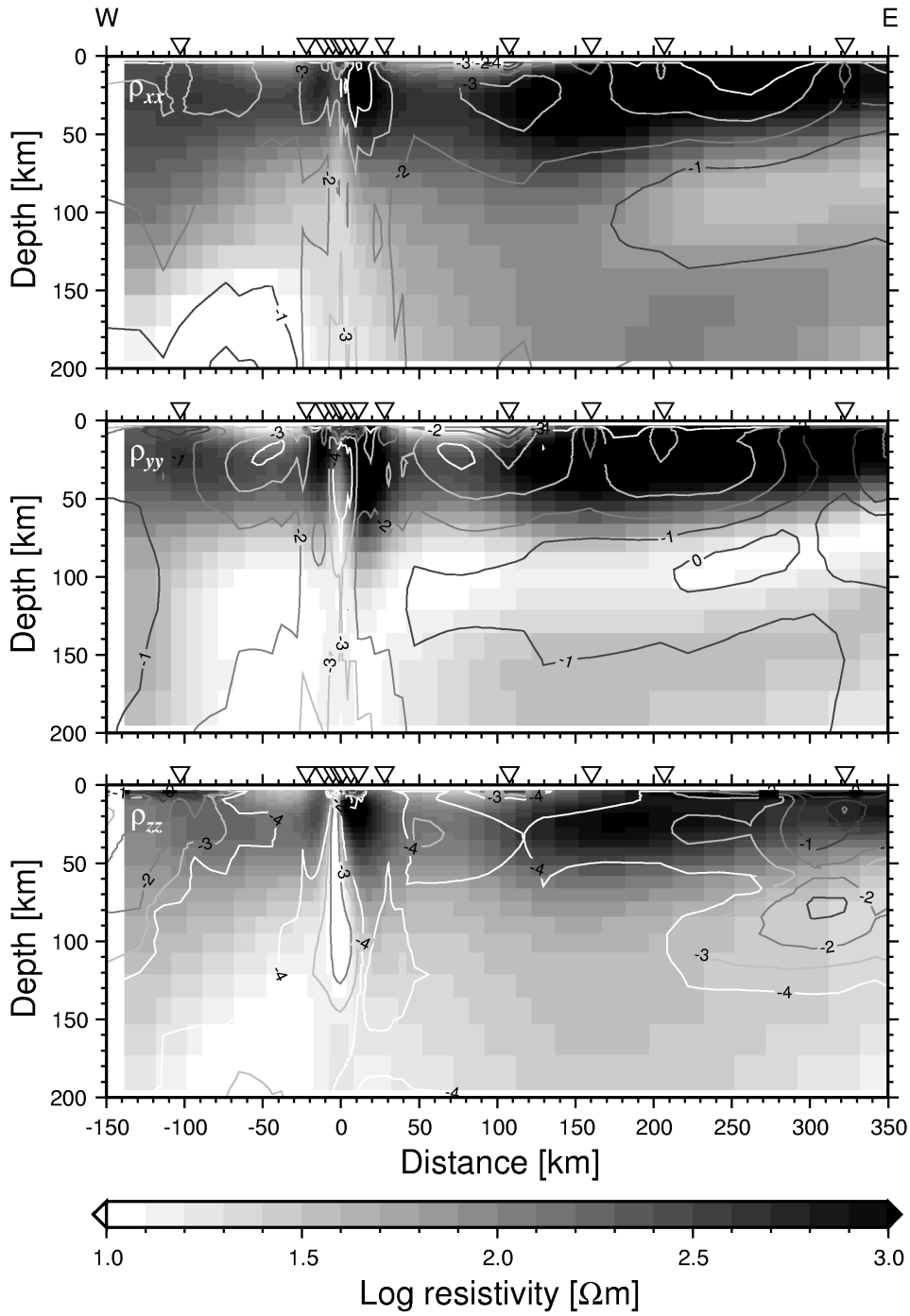

Figure 6. Sensitivity (log $diag(\mathbf{A}^t\mathbf{V}^{-1}\mathbf{A})$) plotted as contour lines on the anisotropic resistivity model. See text for discussion.

[32] The upper 60 km of the mantle is more resistive and apparently more isotropic than at greater depth. In general, MT data are not sensitive to the value of resistivity in a highly resistive region, and this is apparent in the sensitivities in the uppermost 60 km of mantle (Figure 6). Although it is clear from the inversion analysis that the upper 60 km is consistently quite resistive compared to greater depths, it is uncertain whether the resulting isotropy is due to a lack of

Figure 5. Pseudosections of the (left) data and (right) model responses and normalized residuals for the isotropic and anisotropic models. Triangles indicate the locations of the sites. Numbers in the top right corner of the normalized residuals are the RMS misfit of the apparent resistivity or phase of each mode. Numbers in the top left corner of the normalized residuals of the apparent resistivity indicate the RMS misfit of both the apparent resistivity and phase for each mode. The total RMS misfits are also specified above the top panels of the normalized residuals.

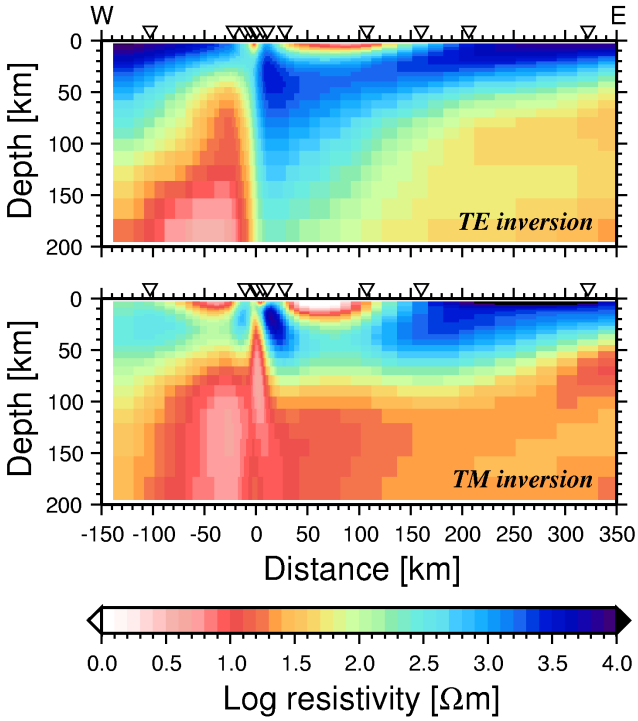

Figure 7. Two-dimensional resistivity models obtained by separate isotropic inversions for the (top) TE and (bottom) TM modes.

sensitivity or is required by the data. A series of significance tests for this were devised, as described by *Evans et al.* [2005]. We use as the initial model a modified version of the preferred anisotropic model in which the upper 60 km is set to be as anisotropic as the deeper mantle. The inversions for various pairs of τ_c and τ_s were then run. The results show that extreme models, for which the closeness constraints are negligible, do retain some anisotropy in the upper 60 km, but the anisotropy is reduced compared to the initial model. Thus, while some upper mantle anisotropy cannot be ruled out, the upper layer is consistently less anisotropic than the structure below 60 km.

[33] Separate inversions of the TE and TM mode data for isotropic structure were attempted to evaluate the origin of features in the isotropic joint inversion model. The inversions were carried out using the anisotropic inversion program to keep algorithmic influence constant, with the error floor of either the TM or TE mode data set to 10,000% to fit only the data for the other mode. τ_c is always set to 10,000 to enforce isotropic resistivity, and τ_s is changed as for the joint inversions. Figure 7 shows the resulting models.

[34] The TE model displays a thick resistive zone immediately east of the ridge, as was seen in the isotropic joint inversion model, while the TM model does not have such a feature (Figures 3a and 7). In the TE-only inversion, the resistive uppermost mantle to the east of the ridge is as thick as for the anisotropic ρ_{xx} model in the early stages of the inversion and becomes thicker at later iterations.

[35] Two-dimensional inversions commonly fit the TM mode more closely than the TE mode response because the latter is more susceptible to breakdown in the assumption of two-dimensionality. Misfit for the TE mode is always worse than for the TM mode responses for all of the inversions carried out in this study (Figure 5). The TM-only inversions, which are more robust against the influence of 3-D structure, as well as the anisotropic joint inversions do not include a thick resistive mantle to the east of the ridge. These observations suggest that the thick resistive mantle results from overfitting TE mode responses that are possibly affected by 3-D structure, and that a resistive mantle down to ~60 km is more likely beneath the MELT survey line.

[36] The sensitivity of the ρ_{zz} model to the sheet conductor is higher than that in surrounding regions and is unimportant elsewhere in the model. However, the peak value of the ρ_{zz} sheet log sensitivity (−1.05) is still about 2 orders of magnitude smaller than the highest value (+1.05) for the ρ_{yy} model, and lies just below the conservative significance level that was selected. This result indicates that the data have some degree of sensitivity to the presence of the sheet, but that it is a secondary model feature. To more fully assess whether the sheet is required, the effect of the choice of initial model on the final inversion result; the contribution of the sheet to the model fit through forward modeling; and the possibility that data from a single site might bias the inversion were evaluated by carrying out a series of jackknife-like inversions in which one data set is eliminated in turn with replacement from the calculation.

[37] The ρ_{zz} inversion may be strongly influenced by the starting model and the closeness constraint because the MT method is less sensitive to vertical conductive features than to horizontal ones. The small sensitivity values for most of the ρ_{zz} model in Figure 6 reflects this. As a result, the gross features of the ρ_{zz} model are similar to those of the ρ_{xx} or ρ_{yy} models. Further, if τ_c is set to 0, the ensuing ρ_{zz} model is very close to the initial half-space model. The only exception occurs at the ridge crest, where the sheet conductor almost always appears with a resistivity that is independent of the starting value.

[38] Forward modeling was carried out for a series of models in which the conductive sheet was progressively shrunk in extent starting at its base and moving upward (Figure 8a). At each step, as a section of sheet was removed, the conductivity below that point was adjusted in order to conserve the vertical conductance within the entire vertical section. The RMS misfit for each model against the depth to the base of the sheet is shown in Figure 8b. As the depth to the base becomes shallower, the RMS misfit systematically increases until it achieves a maximum (2.466) when the sheet is absent. However, the difference between the maximum and minimum misfit values is so small that a double-sided F test is not significant at the 0.35 level. A similar test was applied to the other elements of the conductivity tensor. The RMS misfit for the ρ_{xx} model containing the conductive sheet is 2.655 as compared to the original value of 2.443, for a double-sided F test significance level of 0.01, and hence the data are very sensitive to its presence. However, the misfit to the ρ_{yy} model with the conductive sheet is changed only slightly, indicating that the data are insensitive to the feature. This same conclusion may be derived from the sensitivity values shown in Figure 6.

[39] The MT response for a ρ_{zz} model which has a triangular conductive zone (Figure 8a) was also investigated.

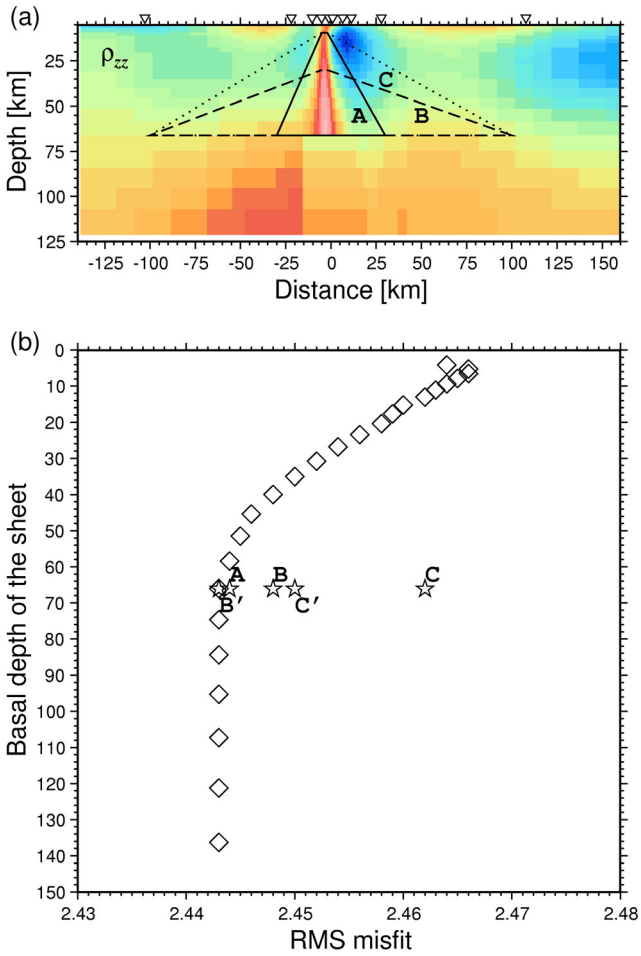

Figure 8. (a) Example of the ρ_{zz} model used for forward modeling. In this model, the conductive sheet extent is reduced to 66 km. Broader conductive zones (A, B, and C) bounded by solid, dashed, and dotted lines, respectively, were also tested through forward modeling. (b) RMS misfits for various patterns of the conductive sheet. The diamonds are for reduced sheet models, and the stars are for the broader conductive zones.

The resistivity values within the triangular area were replaced with 10 Ωm except for the conductive region in the center, where the original value was retained. The RMS misfits for these models are 2.444 for model A (50 km wide at its base), 2.448 for model B (200 km wide at its base but only extending to 30 km depth), and 2.462 for model C (200 km at its base and extending to 10 km depth), respectively (Figure 8b). Further, the effect of asymmetry was checked through models B′ and C′ which are the same as models B and C but with triangular areas only west of the rise axis. The resulting RMS misfits are 2.443 for model B′, which is the same value as that of the best fitting model, and 2.450 for model C′, respectively. None of these changes in RMS misfit are significant at any reasonable confidence level, although a broader region of high conductivity in the shallower parts of the mantle (above about 30 km depth) does affect the RMS misfit more than a narrow one.

[40] Finally, a series of inversions were carried out with one site removed in turn with replacement to assess whether the appearance of the sheet in the models results from overfitting of a particular data set. As the deleted data set is changed, the best smoothness and closeness parameters in the inversion and the convergence process may vary. The inversions were computed 12 times (four combinations of τ_s and τ_c for three different initial models) for each delete-one data set, for a total of 156 inversions. Table 4 indicates whether the sheet is observed in the inversion or not. The models that do not contain the conductive sheet occur for nonoptimal combinations of smoothness and closeness parameters (e.g., those which are either overly smooth or overly isotropic). The conductive sheet appears ubiquitously for all of the delete-one site results when appropriate smoothness and closeness parameters are used. These results indicate that the sheet is not produced because of overfitting of a particular data set, but is a consequence of the data from a diversity of sites.

[41] The above tests show that the data are not very sensitive to the shape of the conductive region, which could be broader than the narrow sheet returned in the inversions. However, some kind of vertical conduit is a consistent rather than a spurious model feature, although the improvement in overall statistical fit from including such a feature is not large.

6. Interpretation and Discussion

[42] The electrical conductivity of the mantle beneath a spreading ridge is controlled by temperature, the presence of interconnected melt, and by mantle composition. In terms of conductivity, these processes are not independent. For example, enhanced temperature under subsolidus conditions will increase electrical conductivity, but will also induce melting when the solidus temperature is exceeded. Unravelling the contributions from each parameter is a challenge, and is best accomplished by first analyzing the regional structure and then looking closely at more localized features in the models.

6.1. Regional Structure

[43] The contribution of temperature on conductivity can be assessed through comparison of the derived structure to that for dry isotropic peridotite based on laboratory measurements [*Xu et al.*, 2000]. The thermal structure is based on a model of a cooling half-space with a basal potential temperature of 1350°C and a mantle adiabat of 0.3°C km^{-1} [*Turcotte and Schubert*, 2002] (Figure 9c). The differences between the log resistivity of the observed structure and the dry model are shown for both the isotropic and anisotropic MELT models in Figures 9a and 9b. The effect of anisotropy on the electrical conductivity of dry olivine is weak (approximately a factor of 2 between the *a* and *c* axes, with the latter being higher), and hence the use of an isotropic reference model with the anisotropic inversion result in Figure 9b does not introduce major interpretation errors.

[44] The most persistent, large-scale feature of the anisotropic inversions is the consistently higher conductivity in the direction of plate spreading below ~60 km depth which occurs from very near the ridge axis to the edge of the model, together with the overlying resistive, electrically isotropic upper lithosphere (Figure 3b). These features are

Table 4. Tests for the Presence of a Conductive Sheet in ρ_{zz}[a]

Deleted Site	$\tau_c = 0.1$ $\tau_s = 3$	$\tau_c = 0.1$ $\tau_s = 2$	$\tau_c = 0$ $\tau_s = 3$	$\tau_c = 0$ $\tau_s = 2$
D			X	X
F	X	X	X	X
G		X	X	X
H		X	X	X
I		X	X	X
J	X		X	
L			X	X
M		X	X	X
N		X	X	X
P	X	X	X	X
Q		X	X	X
R	X	X	X	X
S	X	X	X	X

[a]X indicate that the model obtained for the given set of parameters includes the sheet.

more apparent after subtraction of the dry background structure (Figure 9b). The near constant 60 km depth of this feature and its existence very near the ridge crest are inconsistent with a purely thermal origin [*Evans et al.*, 2005]. For example, the depth to the 1350°C isotherm in Figure 9c varies between ~10–50 km over this age range.

[45] The isotropic result in Figure 9a is even more difficult to reconcile with thermal processes due to the significantly thicker (~130 km) resistive section near the ridge axis which thins rapidly to the east beyond 100 km (or an age of 1.3 Ma). Both the extreme thickening near the ridge crest and the thinning away from the ridge crest are inconsistent with known thermal mechanisms. Instead, this result may be caused by forcing isotropy onto the modeling of an anisotropic fabric.

[46] The layered structure in Figures 3b and 9b is also observed in inversions of Rayleigh and Love wave data from the MELT region [*Conder et al.*, 2002; *Dunn and Forsyth*, 2003] at distances over 100 km (or ages over 1.3 Ma) from the ridge axis. The shear velocity decreases from ~4.5 km s^{-1} below the Moho to 4.1 km s^{-1} at about 70 km, below which the gradient reverses sign. Neither the depth extent of the negative shear wave gradient nor the constancy of the velocity structure with plate age are consistent with thermal models. The anisotropic electrical conductivity and shear wave velocity structures are qualitatively consistent throughout the region [*Evans et al.*, 2005].

[47] A region of enhanced conductivity to the east of the ridge from 70–120 km depth is a required feature of the MT data, and appears in all inversion models at all values of τ_c. In the isotropic model (Figure 9a), the enhanced conductivity is 2–3 times the dry peridotite value. For the best fitting anisotropic model (Figure 9b), higher conductivity is seen in the spreading (y) direction, and is about a factor of 4 above the along-axis (x) value. However, even the lower (along-axis) conductivity is 2–3 times above the dry peridotite estimate, while the across-axis value is over a decade

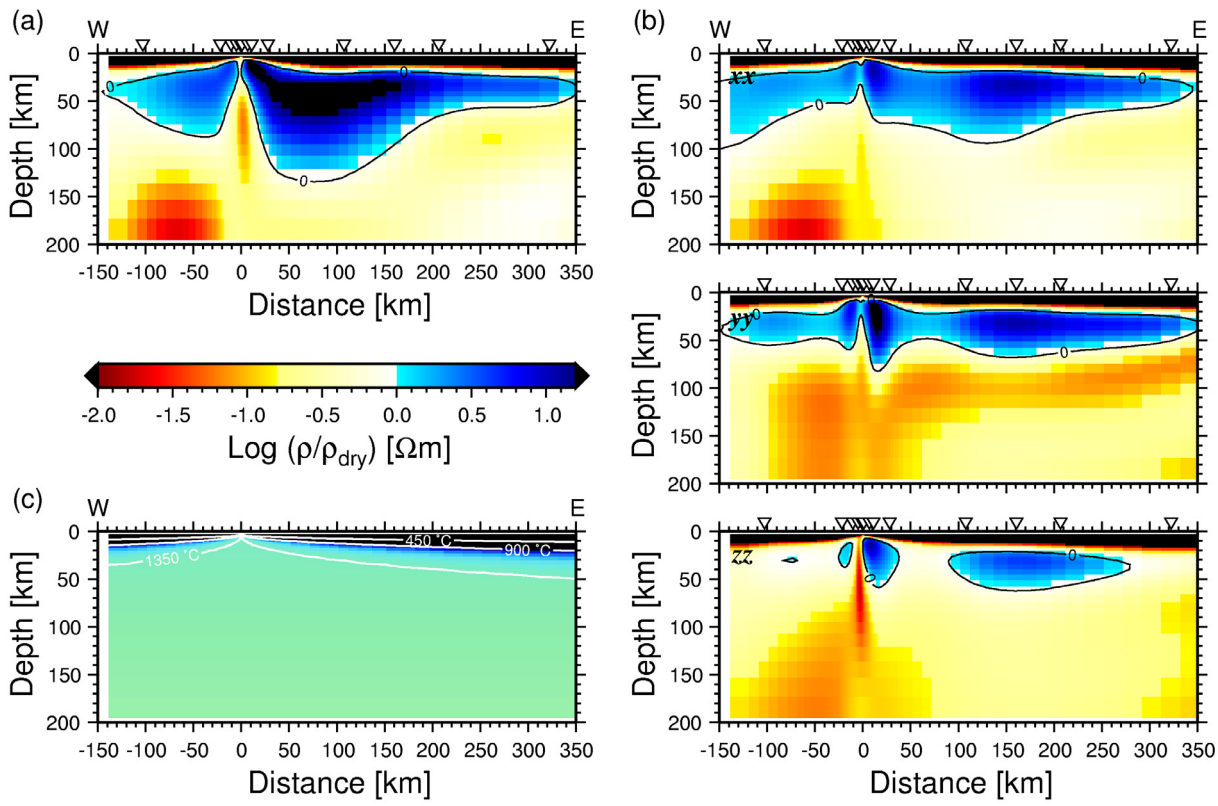

Figure 9. (a) Isotropic and (b) anisotropic resistivity models after subtraction of the dry mantle reference model described in the text. (c) Resistivity model estimated from solid-state experimental measurements with a geotherm based on a half-space cooling model. In Figure 9c, the color indicates log resistivity with the same scale as that in Figure 3, and the contour lines are isotherms.

higher. Unreasonably high (>1500°C) potential temperatures are required to explain any of these observations with thermal structure alone. The vertical (z) conductivity is poorly constrained except immediately below the ridge crest, and will not be further considered as an off-axis constraint.

[48] The conductivity estimate for dry peridotite is substantially higher than the model values at depths shallower than ~60 km for both the isotropic and anisotropic models. However, MT data are insensitive to the actual conductivity value in resistive regions. As a test, forward models were run with a minimum conductivity in the uppermost lithosphere set to the laboratory value at a potential temperature of 1350°C. The fit to the data was not significantly different than was obtained from direct inversion.

[49] *Evans et al.* [2005] present laterally averaged conductivity profiles derived from the anisotropic model in Figure 3b, and compare them to dry mantle estimates. Their calculation assumed that all of the hydrogen is contributing to conductivity enhancement, and thus considered the maximum influence of hydrogen on conductivity. They showed that anisotropic conductivity in the across-axis direction is similar to that predicted from the Nernst–Einstein relation for hydrogen diffusion parallel to the a axis or [100] direction in olivine containing 1000 H/10^6 Si [*Karato*, 1990]. The conductivity in the along-axis direction is significantly smaller even in light of uncertainty in the hydrogen diffusion data. *Evans et al.* [2005] concluded that anisotropy of conductivity can be explained if there is strong lattice preferred orientation of olivine due to flow in the mantle away from the spreading ridge. The observed factor of 4 anisotropy is compatible with about 50% alignment of olivine in the [100] direction [*Simpson*, 2002], and is also consistent with the ~4% anisotropy of Rayleigh waves observed over this depth range. These conclusions are also compatible with the basin-scale bounds in conductivity given by *Lizarralde et al.* [1995], suggesting that a wet region below ~60 km is a major feature of the oceanic mantle.

[50] The off-axis anisotropic structure continues almost undisturbed beneath the ridge axis where melting is active (see Figure 3b). As a result, a wet mantle interpretation, probably including a small amount of melt near the spreading center, is preferred over alternatives, including the presence of melt off axis [*Evans et al.*, 2005]. These conclusions are compatible with the model of *Hirth and Kohlstedt* [1996], who proposed that the redistribution of water due to partial melting controls the rheology of oceanic lithosphere and asthenosphere. Upwelling mantle beneath the rise axis starts to melt when it crosses the wet solidus at ~115 km. The melt fraction is very limited until material crosses the dry solidus at around 60–70 km depth, at which point melting is rapidly enhanced and water is preferentially extracted from the solid phase into the melt. Water remaining in the solid phase would be very limited at melt fractions above 0.5% [*Hirth and Kohlstedt*, 1996; *Aubaud et al.*, 2004]. As a result, wet, low-viscosity mantle material flows on both sides of the rise axis below the dry solidus, while dry, and hence higher-viscosity, mantle material flows above. This model predicts a boundary between a dry and wet mantle at around 60 km, which is in good agreement with the MELT MT data. Further, electrical anisotropy is significantly greater within the conductive region than in the overlying resistive layer, consistent with the lack of significant anisotropy of dry olivine and further supporting the dry–wet transition model.

6.2. Melt Beneath the Ridge

[51] In the vicinity of the rise axis, above a depth of ~70 km where the conductivity is higher than predicted for a dry peridotite mantle, the conductivity enhancement is probably a consequence of partial melting. There are a variety of models with which the impact of melt on bulk conductivity may be estimated [e.g., *Schmeling*, 1986; *Heinson and Constable*, 1992; *Watanabe and Kurita*, 1993; *Roberts and Tyburczy*, 1999]. Most of these relationships refer to an isotropic melt distribution, although results have been derived for ellipsoidal inclusions [*Schmeling*, 1986; *Evans*, 1994] (which can result in anisotropic conductivity), for aligned cracks [*Yu et al.*, 1997], and for sheets [*Roberts and Tyburczy*, 1999], which are often referred to as the parallel bound.

[52] Inference that conductivity in the vertical direction beneath the ridge is different from that in the two horizontal directions immediately suggests differences in the degree of melt interconnection, with melt better connected vertically. However, as was stressed in section 6.1, the conductivity in the vertical component model is not well defined, precluding a tight constraint on the vertically connected melt fraction.

[53] The lowest bound on melt fraction comes from either the connected Hashin–Shtrikman (HS) bound [*Hashin and Shtrikman*, 1962] or the parallel bound for aligned sheets. Given that there is clear evidence for anisotropic conductivity and the HS bounds incorporate an isotropic melt distribution, the melt fraction will be estimated using the parallel bound, although the difference between the two is small. Figure 10 shows the melt fraction for the uppermost mantle in the vicinity of the rise axis estimated from the isotropic and anisotropic conductivity models shown in Figures 3a and 3b. The contour lines in Figure 10 show the minimum melt fraction for the three anisotropic resistivity models. The background mantle conductivity for these relationships was calculated using the laboratory data of *Xu et al.* [2000] as previously discussed but with a linear decrease of 2°C km^{-1} with upwelling superimposed on the original temperature profile between 10 and 60 km depth to account for the influence of latent heat of fusion. The calculation yields the melt conductivity as a function of temperature using the relationship of *Tyburczy and Waff* [1983]. Note that the calculation does not include the effect of mantle hydration on conductivity, so is inherently upward biased by an indeterminate but significant amount, although in all other aspects these values represent lower bounds on melt fraction. The effect of hydration is less likely to be a factor in the upper 60–70 km directly beneath the ridge where water will be preferentially partitioned into the melt, but is more likely to be a factor in regions where melting has been less extensive.

[54] Figure 10 shows that both isotropic and anisotropic models predict that melt will concentrate in the narrow region beneath the ridge. The lower bound on the average melt fraction in the central melt zone is ~4% for the z direction, no more than 1% for the x and y directions, and

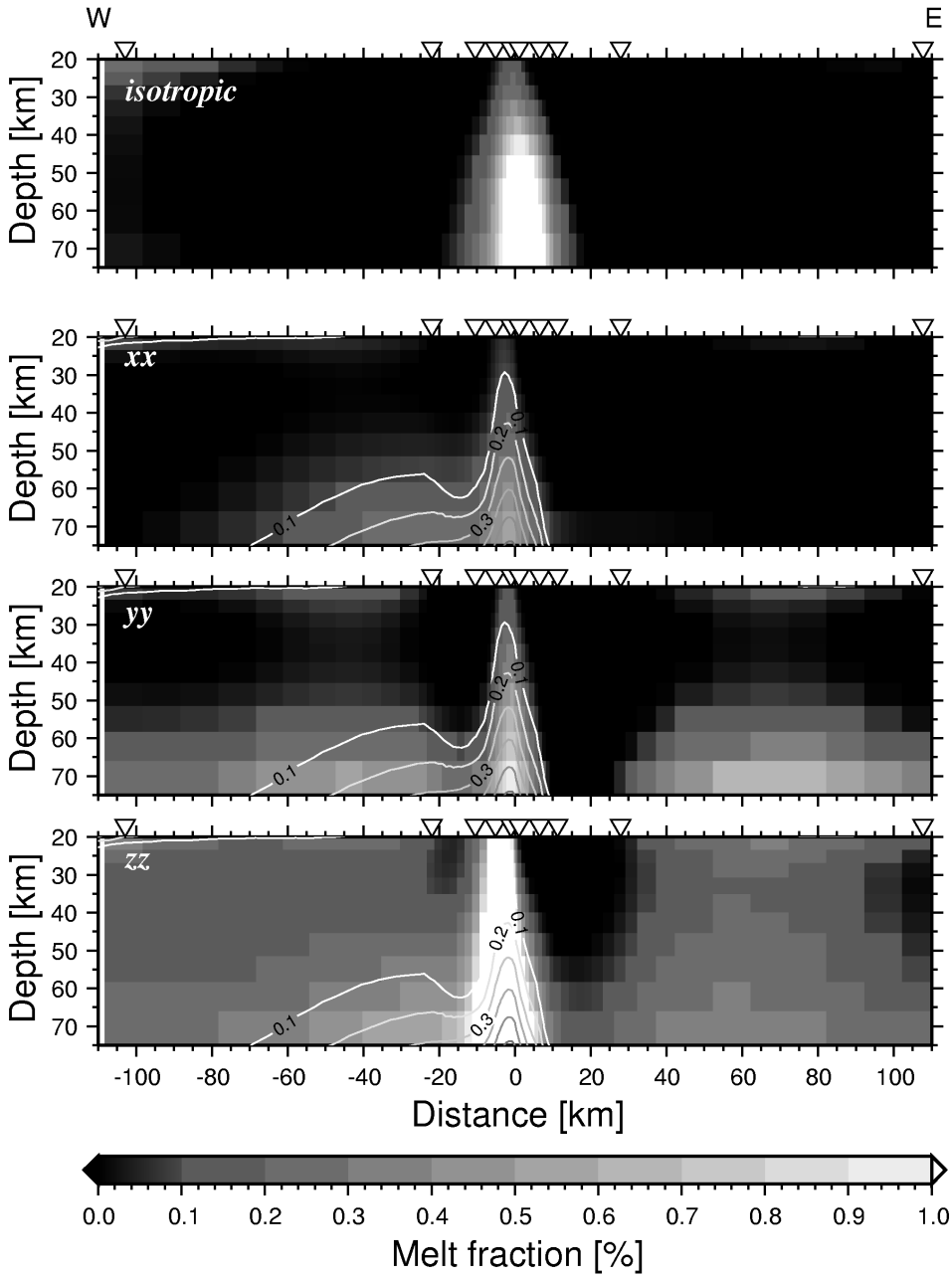

Figure 10. Melt fraction calculated from the isotropic and anisotropic conductivity models shown in Figures 3a and 3b in the vicinity of the rise axis. The contour lines in the bottom three panels are the minimum melt fraction among the three anisotropic models.

~1% for the isotropic model. The larger melt fraction in the vertical direction beneath the ridge can be interpreted as melt in a vertically oriented configuration, such as in vertically aligned tubes. However, one issue with models containing a vertical sheet of melt is that seismic studies do not yield evidence for its existence. For example, *Hung et al.* [2000] ruled out the presence of a narrow melt sheet that has a velocity anomaly width product of more than 2.5 $km^2\ s^{-1}$ (e.g., no larger than 5 km wide with a 0.5 $km\ s^{-1}$ velocity anomaly).

[55] In an effort to estimate the degree of melt connectivity in the horizontal directions, the models of *Schmeling* [1986] and *Watanabe and Kurita* [1993] (which are ultimately derived from *Madden* [1976]) were examined. These results require that the bulk conductivity is the geometric mean of two end-member distributions: one modeled by the upper HS (or parallel) bound which accounts for well-connected melt, and the second resulting from ellipsoidal inclusions which are isolated and hence poorly connected electrically. The two distributions are traded against each other through an exponent which represents the degree of interconnectivity.

[56] Since the vertical conductivity beneath the ridge is highest, it will be assumed that melt is ideally connected in that direction. This scenario yields an estimate of the melt fraction from which the interconnection in the x and y

directions can be derived. Typical values of horizontal interconnection are 80% directly beneath the ridge and 50–60% at depths of 50–70 km and 20–40 km west of the ridge.

[57] The melt region inferred from the anisotropic model is asymmetric and broader to the west than to the east, with very little evidence for melt further than about 10 km to the east of the ridge crest. The asymmetry in melt distribution is not as dramatic as observed in earlier work [e.g., *Evans et al.*, 1999], mainly because of the difference in the deeper resistive structure for the isotropic and anisotropic models. The largest melt fractions are centered about 5 km west of the rise axis in all three coordinate directions. Using isotropic relationships, the melt fraction derived from conductivity along axis is lower than that in the across-ridge direction. Taken at face value, this suggests that melt is better connected in the direction of mantle flow toward the ridge than along strike. Seismic studies identify a zone of 1–2% melt in the top 100 km of mantle extending 150–200 km to the west of the ridge, but melting appears to stop east of the ridge [*Melt Seismic Team*, 1998; *Forsyth et al.*, 1998; *Toomey et al.*, 1998]. *Dunn and Forsyth* [2003] show that the asymmetry in structure extends upward as far as the base of the crust, although it is less pronounced at shallower depths. The inferred melt fraction of up to 1–2% estimated from the seismic study of *Dunn and Forsyth* [2003] is lower than that estimated from the vertical conductivity, but is consistent with the melt fraction estimated from the horizontal conductivities. The melt fraction inferred from the isotropic model is also in good agreement with the seismic study. However, the melt zone is more symmetric with an absence of melt in the broad zone to the west of the ridge, although asymmetry still appears in the resistivity model (Figure 3a).

[58] A small amount of melt over a broad region supports the premise that it must be efficiently and rapidly extracted from the mantle. The inferred differences in interconnection with location also suggest multiple types of melt distribution, with some well connected but also with some sitting in isolated parts of the network. Isotope geochemistry supports a model in which melt transport occurs through a mix of flow in focused, high-porosity conduits and percolation through a porous medium [*Sims et al.*, 2002]. *Jull et al.* [2002] estimate that ~60% of the total melt flux occurs by porous flow, while 40% travels through high-porosity channels that occupy only a small percentage of the mantle volume that undergoes melting. Mixing of the two melt populations is predicted to occur at the top of the melting column at depths shallower than the MT data are able to resolve.

[59] The existence of an asymmetric but broad melting region beneath the southern East Pacific Rise has presented a challenge for modeling of mantle flow and melt generation. *Toomey et al.* [2002] and *Conder et al.* [2002] attempted to simulate mantle flow in the presence of asymmetric plate motion, and postulated the existence of a high-temperature anomaly and eastward moving pressure-driven flow west of the ridge axis which represents return flow from the Pacific superswell region. The flow pattern in the deep mantle in these models is dominantly west-east with gentle upwelling beneath the ridge. The mantle to the west of the ridge crest and 100–200 km deep is highly conductive in both the along- and across-axis directions (Figures 3b and 9b), although MT data are limited west of the ridge, so this conclusion is tenuous. These features may be interpreted as a high-temperature region, and hence are consistent with the premise that the mantle is hotter to the west of the ridge crest to a depth of 200–300 km, in rough agreement with the models of *Toomey et al.* [2002] and *Conder et al.* [2002].

[60] The abrupt drop in melt fraction to the east of the ridge has also been observed in seismic data. As previously discussed, thermal mechanisms alone cannot explain the conductivity structure seen in resistivity models across the ridge axis. *Dunn and Forsyth* [2003] suggest that a component of downwelling flow occurs to the east of the ridge, potentially refreezing any residual melt that is carried along. They also suggest that melt could be focused to the ridge axis along the base of an impermeable layer. It is possible that the resistive upper layer in the resistivity model images such a boundary near the ridge axis.

7. Conclusions

[61] Results from a more detailed analysis of the MELT EM data have been presented. Two newly developed approaches were applied to an enhanced version of the data set: (1) more accurate correction for the effects of topography on the MT responses and (2) inversion for 2-D anisotropic structure. The latter incorporates both variable smoothness and variable closeness of the along-strike, cross-strike, and vertical conductivities and hence allows model space to be explored for preferred structures.

[62] The inversion analysis showed that the best fitting anisotropic resistivity model provides only a slightly better fit to the data than the best fitting isotropic resistivity model. Although it is difficult to choose the anisotropic model from statistical analysis of the MT data alone, consistency with many other observations suggest that the anisotropic model is correct. The anisotropic model displays four key features: (1) a more conductive mantle in the cross-strike direction to the east of the rise axis at depths of 60–120 km, (2) an isotropic, highly resistive lithosphere shallower than 60 km, (3) a resistive-conductive boundary that is independent of lithospheric age, and (4) a narrow, highly conductive sheet in the vertical (and to a lesser extent, along ridge) conductivity located immediately beneath the rise axis. The first three features are very well resolved by the data.

[63] The most prominent features of the resistivity structure at distances 100 km or more off axis are interpreted in terms of mantle hydration in conjunction with the presence of lattice preferred orientation below 60 km together with an overriding resistive layer that has been dehydrated due to melting processes associated with ridge accretion. Near the ridge axis, enhanced conductivity of the mantle below 60 km can be explained by the presence of at most 1% partial melt on the basis of the better constrained horizontal conductivities. A conductive sheet in the vertical conductivity models suggests that the melt is more highly concentrated and connected in the vertical direction immediately beneath the rise axis, although forward modeling shows that details of this feature are not well resolved. The melt zone is at least 100 km wide and is asymmetric, having a greater extent to the west. In fact, there is no evidence for melt to

the east of the ridge at distances greater than about 10 km off axis.

[64] **Acknowledgments.** We thank Shun-ichiro Karato and two anonymous referees for their considerate advice which improved the manuscript. All figures were produced using the GMT software of *Wessel and Smith* [1998]. This work was supported by NSF grant OCE0118254 and the Research Program on Mantle Core Dynamics, Institute for Research on Earth Evolution (IFREE), Japan Agency for Marine-Earth Science and Technology (JAMSTEC).

References

Aubaud, C., E. H. Hauri, and M. M. Hirschmann (2004), Water partition coefficients between nominally anhydrous minerals and basaltic melts, *Geophys. Res. Lett.*, *31*(20), L20611, doi:10.1029/2004GL021341.

Baba, K., and A. D. Chave (2005), Correction of seafloor magnetotelluric data for topographic effects during inversion, *J. Geophys. Res.*, *110*, B12105, doi:10.1029/2004JB003463.

Baba, K., and N. Seama (2002), A new technique for the incorporation of seafloor topography in electromagnetic modeling, *Geophys. J. Int.*, *150*, 392–402.

Braun, M. G., G. Hirth, and E. M. Parmentier (2000), The effects of deep damp melting on mantle flow and melt generation beneath mid-ocean ridges, *Earth Planet. Sci. Lett.*, *176*, 339–356.

Buck, W. R., and W. Su (1989), Focused mantle upwelling below mid-ocean ridges due to feedback between viscosity and melting, *Geophys. Res. Lett.*, *16*(7), 641–644.

Chave, A. D., and J. T. Smith (1994), On electric and magnetic galvanic distortion tensor decompositions, *J. Geophys. Res.*, *99*, 4669–4682.

Chave, A. D., and D. J. Thomson (2003), A bounded influence regression estimator based on the statistics of the hat matrix, *J.R. Stat. Soc., Ser. C*, *52*, 307–322.

Chave, A. D., and D. J. Thomson (2004), Bounded influence estimation of magnetotelluric response functions, *Geophys. J. Int.*, *157*, 988–1006, doi:10.1111/j.1365-246X.2004.02203.x.

Chave, A. D., J. R. Booker, J. T. Smith, and C. Aprea (1992), Model study for a mid-ocean ridge magnetotelluric transect, *Eos Trans. American Geophysical Union*, *73*, 313.

Chave, A. D., R. L. Evans, J. G. Hirth, P. Tarits, R. L. Mackie, J. R. Booker and The MELT Team (2001), Anisotropic electrical structure beneath the East Pacific Rise at 17°S, paper presented at Long-term observations in the oceans: Current status and perspectives for the future, OHP/ION Joint Symposium, Yamanashi Prefecture, Japan.

Conder, J. A., D. W. Forsyth, and E. M. Parmentier (2002), Asthenospheric flow and asymmetry of the East Pacific Rise, MELT area, *J. Geophys. Res.*, *107*(B12), 2344, doi:10.1029/2001JB000807.

Constable, S. C., T. J. Shankland, and A. Duba (1992), The electrical conductivity of an isotropic olivine mantle, *J. Geophys. Res.*, *97*, 3397–3404.

Dunn, R. A., and D. W. Forsyth (2003), Imaging the transition between the region of mantle melt generation and the crustal magma chamber beneath the southern East Pacific Rise with short period Love waves, *J. Geophys. Res.*, *108*(B7), 2352, doi:10.1029/2002JB002217.

Evans, R. L. (1994), Constraints on the large scale porosity of young oceanic crust from seismic and resistivity data, *Geophys. J. Int.*, *119*, 869–879.

Evans, R. L., and M. E. Everett (1992), Magnetotellurics and mid-ocean ridge melt transport: A 2-d perspective, in *Mantle Flow and Melt Generation at Mid-Ocean Ridges*, *Geophys. Monogr. Ser.*, vol. 71, edited by J. P. Morgan, D. K. Blackman, and J. M. Sinton, pp. 353–361, AGU, Washington, D. C.

Evans, R. L., et al. (1999), Asymmetric electrical structure in the mantle beneath the East Pacific Rise at 17°S, *Science*, *286*, 752–756.

Evans, R. L., G. Hirth, K. Baba, D. Forsyth, A. Chave, and R. Mackie (2005), Geophysical evidence from the MELT area for compositional controls on oceanic plates, *Nature*, *437*, 249–252, doi:10.1038/nature04014.

Forsyth, D. W., S. C. Webb, L. M. Dorman, and Y. Shen (1998), Phase velocities of Rayleigh waves in the MELT experiment on the East Pacific Rise, *Science*, *280*, 1235–1238.

Groom, R. W., and R. C. Bailey (1989), Decomposition of magnetotelluric impedance tensors in the presence of local three-dimensional galvanic distortion, *J. Geophys. Res.*, *94*, 1913–1925.

Hammond, W. C., and D. R. Toomey (2003), Seismic velocity anisotropy and heterogeneity beneath the Mantle ELectromagnetic and Tomography Experiment (MELT) region of the East Pacific Rise from analysis of *P* and *S* body waves, *J. Geophys. Res.*, *108*(B4), 2176, doi:10.1029/2002JB001789.

Hashin, Z., and S. Shtrikman (1962), A variational approach to the theory of effective magnetic permeability of multiphase materials, *J. Appl. Phys.*, *33*, 3125–3131.

Heinson, G., and S. Constable (1992), The electrical conductivity of the oceanic upper mantle, *Geophys. J. Int.*, *110*, 159–179.

Heinson, G., and F. E. M. Lilley (1993), An application of thin-sheet electromagnetic modeling to the Tasman Sea, *Phys. Earth Planet. Inter.*, *81*, 231–251.

Hirth, G., and D. L. Kohlstedt (1996), Water in the oceanic upper mantle: Implications for rheology, melt extraction and the evolution of the lithosphere, *Earth Planet. Sci. Lett.*, *144*, 93–108.

Huang, X., Y. Xu, and S. Karato (2005), Water content in the transition zone from electrical conductivity of wadsleyite and ringwoodite, *Nature*, *434*, 746–749.

Hung, S. H., D. W. Forsyth, and D. R. Toomey (2000), Can a narrow, melt-rich, low-velocity zone of mantle upwelling be hidden beneath the East Pacific Rise? limits from waveform modeling and the MELT Experiment, *J. Geophys. Res.*, *105*(B4), 7945–7960.

Jull, M., P. Kelemen, and K. Sims (2002), Consequences of diffuse and channelled porous melt migration on uranium series disequilibria, *Geochim. Cosmochim. Acta*, *66*, 4133–4148.

Karato, S. (1990), The role of hydrogen in the electrical conductivity of the upper mantle, *Nature*, *347*, 272–273.

Kohlstedt, D. L., and S. J. Mackwell (1998), Diffusion of hydrogen and intrinsic point defects in olivine, *Z. Phys. Chem.*, *207*, 147–162.

Lizarralde, D., A. Chave, G. Hirth, and A. Schultz (1995), Northeastern Pacific mantle conductivity profile from long-period magnetotelluric sounding using Hawaii-to-California submarine cable data, *J. Geophys. Res.*, *100*, 17,837–17,854.

Madden, T. R. (1976), Random networks and mixing laws, *Geophysics*, *41*, 1104–1125.

MELT Seismic Team (1998), Imaging the deep seismic structure beneath a mid-ocean ridge: The MELT experiment, *Science*, *280*, 1215–1218.

Nolasco, R., P. Tarits, J. H. Filloux, and A. D. Chave (1998), Magnetotelluric imaging of the Society Islands hotspot, *J. Geophys. Res.*, *103*, 30,287–30,309.

Parker, R. L., and J. R. Booker (1996), Optimal one-dimensional inversion and bounding of magnetotelluric apparent resistivity and phase measurements, *Phys. Earth Planet. Inter.*, *98*, 269–282.

Roberts, J. J., and J. A. Tyburczy (1999), Partial-melt electrical conductivity: Influence of melt composition, *J. Geophys. Res.*, *104*, 7055–7065.

Rodi, W., and R. L. Mackie (2001), Nonlinear conjugate gradients algorithm for 2-D magnetotelluric inversion, *Geophysics*, *66*, 174–187.

Scheirer, D. S., D. W. Forsyth, M. H. Cormier, and K. C. Macdonald (1998), Shipboard geophysical indications of asymmetry and melt production beneath the East Pacific Rise near the MELT experiment, *Science*, *280*, 1221–1224.

Schmeling, H. (1986), Numerical models on the influence of partial melt on elastic, anelastic, and electrical properties of rocks, part II: Electrical conductivity, *Phys. Earth. Planet. Inter.*, *43*, 123–136.

Scott, D. R., and D. J. Stevenson (1989), A self-consistent model of melting, magma migration and buoyancy-driven circulation beneath mid-ocean ridges, *J. Geophys. Res.*, *94*, 2973–2988.

Simpson, F. (2002), Intensity and direction of lattice-preferred orientation of olivine: Are electrical and seismic anisotropies of the Australian mantle reconcilable?, *Earth Planet. Sci. Lett.*, *203*, 535–547.

Sims, K. W. W., et al. (2002), Chemical and isotopic constraints on the generation and transport of magma beneath the East Pacific Rise, *Geochim. Cosmochim. Acta*, *66*, 3481–3504.

Small, C., and L. V. Danyushevsky (2003), Plate-kinematic explanation for mid-oceanic-ridge depth discontinuities, *Geology*, *31*(5), 399–402.

Smith, W. H., and D. T. Sandwell (1994), Bathymetric prediction from dense altimetry and sparse shipboard bathymetry, *J. Geophys. Res.*, *99*, 21,803–21,824.

Spiegelman, M., and D. McKenzie (1987), Simple 2-D models for melt extraction at mid-ocean ridges and island arcs, *Earth Planet. Sci. Lett.*, *83*, 137–152.

Thomson, D. J.. and A. D. Chave (1991), Jackknife error estimates for spectra, coherences, and transfer functions, in *Advances in Spectral Analysis and Array Processing*, vol. 1, edited by S. Haykin, pp. 58–113, Prentice-Hall, Upper Saddle River, N. J.

Toomey, D. R., W. S. D. Wilcock, S. C. Solomon, W. C. Hammond, and J. A. Orcutt (1998), Mantle seismic structure beneath the MELT region of the East Pacific Rise from *P* and *S* wave tomography, *Science*, *280*, 1224–1227.

Toomey, D. R., W. S. D. Wilcock, J. A. Conder, D. W. Forsyth, J. D. Blundy, E. M. Parmentier, and W. C. Hammond (2002), Asymmetric mantle dynamics in the MELT region of the East Pacific Rise, *Earth Planet. Sci. Lett.*, *200*, 287–295.

Turcotte, D. L., and C. Schubert (2002), *Geodynamics*, 2nd ed., 456 pp., Cambridge Univ. Press, New York.

Tyburczy, J. A., and H. S. Waff (1983), Electrical conductivity of molten basalt and andesite to 25 kilobars pressure: Geophysical significance and implications for charge transport and melt structure, *J. Geophys. Res.*, *88*, 2413–2430.

Wannamaker, P. E., et al. (1989), Magnetotelluric observations across the Juan de Fuca subduction system in the EMSLAB project, *J. Geophys. Res.*, *94*, 14,111–14,125.

Watanabe, T., and K. Kurita (1993), The relationship between electrical conductivity and melt fraction in a partially molten simple system: Archie's law behavior, *Phys. Earth Planet. Inter.*, *78*, 9–17.

Wessel, P., and W. H. F. Smith (1998), New, improved version of the generic mapping tools released, *Eos Trans. AGU*, *79*, 579.

Wolfe, C. J., and S. C. Solomon (1998), Shear-wave splitting and implications for mantle flow beneath the MELT region of the East Pacific Rise, *Science*, *280*, 1230–1232.

Xu, Y., T. J. Shankland, and B. T. Poe (2000), Laboratory-based electrical conductivity in the Earth's mantle, *J. Geophys. Res.*, *105*, 27,865–27,875.

Yu, L., R. L. Evans, and R. N. Edwards (1997), Transient electromagnetic responses in seafloor with tri-axial anisotropy, *Geophys. J. Int.*, *129*, 292–304.

K. Baba, Earthquake Research Institute, University of Tokyo, 1–1–1, Yayoi, Bunkyo-ku, Tokyo, 113–0032, Japan. (kbaba@eri.u-tokyo.ac.jp)

A. D. Chave, Department of Applied Ocean Physics and Engineering, Woods Hole Oceanographic Institution, Woods Hole, MA 02543, USA. (alan@whoi.edu)

R. L. Evans, Department of Geology and Geophysics, Woods Hole Oceanographic Institution, Woods Hole, MA 02543, USA. (revans@whoi.edu)

G. Hirth, Department of Geology and Geophysics, Woods Hole Oceanographic Institution, Woods Hole, MA 02543, USA. (ghirth@whoi.edu)

R. L. Mackie, GSY-USA, Inc., PMB 643, 2261 Market St., San Francisco, CA 94114, USA. (randy@gsy-usa.com)